

See Eye to Eye: A Lidar-Agnostic 3D Detection Framework for Unsupervised Multi-Target Domain Adaptation

Darren Tsai

Julie Stephany Berrio

Mao Shan

Stewart Worrall

Eduardo Nebot

University of Sydney

{d.tsai, j.berrio, s.worrall, m.shan, e.nebot}@acfr.usyd.edu.au.

Abstract

Sampling discrepancies between different manufacturers and models of lidar sensors result in inconsistent representations of objects. This leads to performance degradation when 3D detectors trained for one lidar are tested on other types of lidars. Remarkable progress in lidar manufacturing has brought about advances in mechanical, solid-state, and recently, adjustable scan pattern lidars. For the latter, existing works often require fine-tuning the model each time scan patterns are adjusted, which is infeasible. We explicitly deal with the sampling discrepancy by proposing a novel unsupervised multi-target domain adaptation framework, *SEE*, for transferring the performance of state-of-the-art 3D detectors across both fixed and flexible scan pattern lidars without requiring fine-tuning of models by end-users. Our approach interpolates the underlying geometry and normalizes the scan pattern of objects from different lidars before passing them to the detection network. We demonstrate the effectiveness of *SEE* on public datasets, achieving state-of-the-art results, and additionally provide quantitative results on a novel high-resolution lidar to prove the industry applications of our framework. This dataset and our code will be made publicly available.

1. Introduction

3D object detection is a fundamental task that allows perception systems to build an awareness of the environment with applications in mixed reality, collaborative robots, and autonomous driving. The release of large-scale, annotated public autonomous driving datasets [6, 16, 51] has quickened the pace of 3D detection research, with novel architectures [19, 46] consistently reaching greater heights on the leaderboards. Alongside software advances, lidar manufacturing has recently made outstanding progress with innovative sensor architectures and scan patterns; however, state-of-the-art (SOTA) detection architectures are not directly

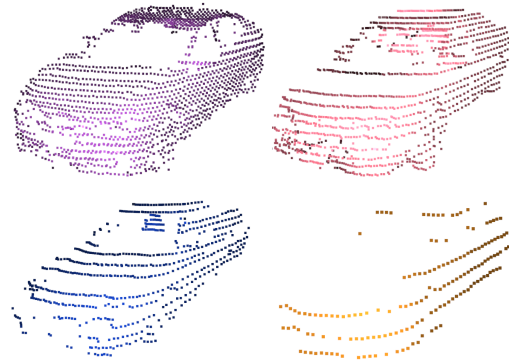


Figure 1. Sampling discrepancy of cars at 10m distance captured by different lidars. Top left: Baraja Spectrum-Scan™, an adjustable scan pattern lidar; Top right: Waymo Open Dataset [51] (64-beam); Bottom left: KITTI Dataset [16] (64-beam); Bottom right: nuScenes Dataset [6] (32-beam). All figures are best viewed in colour.

transferable to different lidar scan patterns [64, 66, 71].

Each lidar has a distinct scan pattern, leading to a representation of objects specific to its scan pattern (Figure 1). This characteristic of lidars results in performance degradation when models trained for one lidar are tested on other types of lidars. In the supervised machine learning paradigm, this would require substantial effort to acquire manually annotated data for the new lidar scan pattern and to subsequently fine-tune the network. Approaches therefore that adapt a trained lidar domain to an unseen test domain are highly attractive for industry applications where it is costly to obtain labelled data.

Lidars often come in a variety of configurations, and some, like the Baraja Spectrum-Scan™, can adjust their scan pattern in real-time. Yang *et al.* [64] proposed a self-training approach using a memory-bank strategy to generate high-quality pseudo-labels. This approach is highly effective when transferring the performance of the SOTA from one labelled, fixed scan pattern lidar to a separate non-

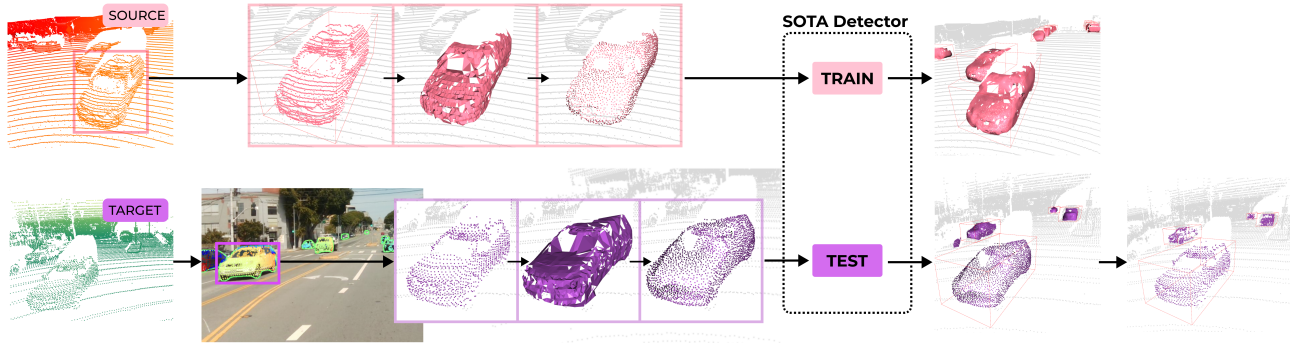


Figure 2. Overview of SEE, our lidar-agnostic unsupervised multi-target DA framework for 3D object detection. Our framework allows a 3D detector trained on one source domain to be used on multiple target domains without additional training.

labelled, fixed scan pattern lidar. However, for lidars that have adjustable scan patterns, this would require fine-tuning a new model for each adjusted scan pattern, which is impractical. The motivation for this approach, therefore, is to explore a scan pattern agnostic representation of objects to enable a trained 3D detector to perform on any lidar scan pattern.

We propose an unsupervised multi-target domain adaptation (DA) framework, SEE, that works on both fixed and adjustable scan pattern lidars without requiring fine-tuning a model for each new scan pattern. SEE enables the performance of SOTA models, trained on a single lidar dataset (source domain), to be adapted for multiple unlabelled lidar datasets of various, distinct scan patterns (target domains). Our approach focuses on transforming objects in their lidar-specific representation, to a scan pattern agnostic representation. We subsequently feed this into any SOTA detector and in so doing, we alleviate the bias towards a specific lidar’s object representation.

Our framework is comprised of 3 phases: object isolation, surface completion (SC), and point sampling. In the first phase, we use ground-truth boxes and image instance segmentation to isolate object points. Thereafter, we use the Ball-pivoting algorithm [3] to interpolate the triangle mesh of the isolated point cloud. From this geometric representation, the third phase is to sample from the triangle mesh using Poisson disk sampling [70]. The detector is subsequently trained on this sampled representation to alleviate the bias of the source domain scan pattern.

Extensive experimentation using two SOTA detectors, SECOND [61] and PV-RCNN [46], on multiple public datasets and a manually labelled, novel lidar dataset validates the efficacy of our framework. For instance, without domain adaptation, SECOND and PV-RCNN obtain an AP_{3D} 0.7 IoU score of 11.95 and 37.30, respectively, when trained on the Waymo open dataset [51] and tested on the KITTI dataset [16]. With SEE, the same models obtained

a performance increase in 3D Average Precision (AP) of $11.95 \rightarrow 65.01$ and $37.30 \rightarrow 78.89$, which is an improvement over the state-of-the-art [64] of 3.59 and 7.01 AP, respectively. We additionally prove the industry applications of our framework by quantitatively demonstrating the transferability of SECOND and PV-RCNN from Waymo and nuScenes to a novel high-resolution lidar, Baraja Spectrum-Scan™.

Contributions. Our main contribution, SEE, as shown in Figure 2, is a simple and effective framework that enables easy adoption of SOTA detectors for any kind of scan pattern. Through comprehensive experimentation, we demonstrate that SEE has the following advantages:

- **Scan Pattern Agnostic:** Significant improvements achieved when transferring the performance of 3D detectors across lidars regardless if the lidar scan pattern is fixed or adjustable.
- **Easy Adoption:** Being a multi-target domain adaptation approach, 3D detections can easily be obtained for new lidars without requiring fine-tuning for each new scan pattern.
- **Detection Performance:** SEE outperforms SOTA on the Waymo \rightarrow KITTI task on all evaluated models.
- **Industry Applicability:** Novel lidars from industry often differ from popular lidars used in the research context. SEE can support new lidars produced by industry; we prove this on a novel, adjustable scan pattern lidar.
- **Versatile:** SEE is compatible with a variety of 3D detectors and 2D instance segmentation networks without modifications to their existing architecture.

2. Related Works

3D Object Detection. The goal of 3D object detection is to obtain the category and location (given in bounding box

corner coordinates, or box centroid and dimensions) of all objects in the scene. Previous works can be categorised into lidar-based and multi-sensor methods. In lidar-based methods, point clouds are commonly converted to 2D representations such as birds-eye-view (BEV) [10, 12, 24, 62] or front-view (FV) [10, 27]. These representations are then fed into 2D CNN architectures to regress bounding box locations and categories. Another popular lidar-based approach explores various representations of points using 3D convolutional networks such as voxels [11, 61, 65, 74], spheres [32, 46], pillars [25], or learning point features directly [35, 47] using point operators [39, 40]. These features are transformed to a BEV feature map where 3D boxes are generated using sparse convolution or transformer architectures [33, 35].

For the multi-sensor approach, some methods [10, 24] propose to fuse 2D point cloud representations (BEV and FV) with the raw image. Other works use image semantic segmentation [55] or detection [38, 58] as priors for their proposed architectures. Pang *et al.* [36] used an IoU-based approach to combine the detections of an image-based and lidar-based detector. For experimentation, we validate our framework on 3D detectors, PV-RCNN [46] and a modified version of SECOND [61], named SECOND-IoU by [64].

Unsupervised Domain Adaptation. In supervised machine learning, the assumption is that the training and testing data are drawn from the same underlying distribution; however, this is often violated in practice. The goal of unsupervised multi-target DA is to address this distribution shift, to learn from a single labelled source domain in such a way that performs well on multiple unlabelled target domains. In this paper, “source domain” refers to the labelled point cloud dataset used for training; “target domain” refers to an unlabelled dataset with a different, unseen lidar. Domain-invariant feature representation is a popular line of work where divergence minimization is used to align the domains during training using adversarial training [15, 44, 45, 54], or divergence measures such as maximum mean discrepancy [18, 31, 42, 50], correlation alignment [34, 49, 57, 72], and contrastive domain discrepancy [22]. Other methods have opted to find a mapping from one domain to another to generate pseudo-target data for training with the known source labels [5, 8, 20, 30].

Specific to DA for point clouds, recent works have addressed the domain shift for semantic segmentation [2, 21, 26, 59, 66, 73], weather interference [60], time-of-day [71], reconstruction [1] and shape classification [41]. For the specific task of labelled source domain to unlabelled target domain for 3D object detection across distinct lidar scan patterns, research has been more sparse. Wang *et al.* [56] proposed a semi-supervised approach using object-size statistics of the target domain to resize training samples in the labelled source domain. A popular approach is the use of

self-training [43, 63, 64, 67] with a focus on generating quality pseudo-labels using temporal information [43, 67] or an IoU scoring criterion for historical pseudo-labels [63, 64]. In particular, while Yang *et al.* [63, 64] has drastically improved the performance over previous works, it is not practical for a lidar that can adjust its scan pattern in real-time. The method would need to be fine-tuned for every adjustment of the scan pattern, and in practice, this fine-tuned model would need to be constantly swapped according to the adjusted scan. This also limits the potential of having a flexible scan pattern in the first place. Conversely, we propose a novel framework that does not require fine-tuning for each new lidar and achieves state-of-the-art performance without any labels or object statistics in the target domain.

3. Method

In this paper, we propose SEE, a framework to adapt a 3D detector trained on labelled source point clouds, to unlabelled target point clouds, each with its distinct scan patterns. We note that our framework is applicable for one source to both single and multi-target DA scenarios.

3.1. Overview and notations

Formally, we denote the point cloud as a set of unordered points $\mathbf{X}_i = \{p_j |_{j=1}^{N_j}\}$, where p_j is the j -th point in the i -th point cloud \mathbf{X}_i with N_j number of points. Each labelled point cloud has a set of annotations $\mathbf{Y}_i = \{y_k |_{k=1}^{N_k}\}$ for N_k objects, where y_k is the k -th bounding box, parameterised by the center (c_x, c_y, c_z) , dimensions (l, w, h) and rotation θ_z around the world frame Z-axis. The point set of all object instances in the point cloud can be represented as $\mathbf{O}_i = \{o_k |_{k=1}^{N_k}\}$, where o_k refers to the points of the k -th object. In this UDA scenario, we denote the source domain as $\chi^S = \{(\mathbf{X}_i^S, \mathbf{Y}_i^S) |_{i=1}^{N^S}\}$, where each i -th point cloud \mathbf{X}_i^S , has a corresponding annotation \mathbf{Y}_i^S for all N^S frames in the source domain. For the target domain, we are given a set of unlabelled point clouds $\chi^T = \{\mathbf{X}_i^T |_{i=1}^{N^T}\}$, where \mathbf{X}_i^T is the i -th point cloud in the target domain with a total number of N^T point clouds.

SEE explicitly bridges the domain gap between distinct scan patterns by transforming only the object instances into a normalized representation. We call this resultant point cloud a semi-canonical domain where only the objects \mathbf{O}_i^S and \mathbf{O}_i^T reside inside a canonical domain. This can be represented by $\mathbf{M}_i^S = \psi(\mathbf{O}_i^S)$ and $\mathbf{M}_i^T = \psi(\mathbf{O}_i^T)$ where \mathbf{M}_i^S and \mathbf{M}_i^T represent the i -th semi-canonical point cloud. We train the 3D object detector $\rho(\mathbf{M}_i^S)$ on this semi-canonical source domain using labels \mathbf{Y}_i^S , and subsequently, in testing, apply it to the semi-canonical target domain $\rho(\mathbf{M}_i^T)$ to obtain bounding boxes which can then be projected back into the target domain \mathbf{X}_i^T . In this paper, the term “rings” is used interchangeably with beams (e.g., KITTI lidar has 64

beams/rings).

3.2. Isolating the Object Point Cloud

The first phase of SEE depicted aims to isolate the object points \mathbf{O}_i^S and \mathbf{O}_i^T in the point cloud. Where labels are available in the source domain, this can easily be accomplished for each k -th object by cropping the point cloud with their bounding box y_k . In the target domain, we utilize instance segmentation to isolate object instances $\mathbf{O}_i^T = \sigma(\mathbf{x}_i^T)$.

Instance segmentation. Using image instance segmentation, we can obtain a mask that outlines the object shape within the detected bounding box. We first project the point cloud into the image plane using the homogenous transformation matrix $T_{\text{camera} \leftarrow \text{lidar}}$ and the camera matrix. Thereafter, in the image plane, we isolate the points within each mask.

Instance segmentation masks allow for tight bounds on the object, giving better isolation of object points over bounding boxes; but this is not without its issues [4]. Viewpoint misalignment of camera and lidar, loosely fitted instance masks, as well as calibration errors [53] can lead to the inclusion of points within the mask that do not belong to the object, shown in Figure 3. Additionally, due to the lack of depth in images, instance segmentation may occasionally pick up cars or people in posters and billboards [17], which is not of interest to 3D object detection for autonomous driving. If these are transformed to the canonical domain and passed into the 3D detector for training, the model would learn the idiosyncrasies and failures specific to a particular instance segmentation model used for generating training data. To bypass this issue, we opt to use instance segmentation only in the target domain which in turn gives our framework flexibility in our choice of instance segmentation models. By using instance segmentation only in the target domain, we make sure that we feed the source domain trained model with clean data.

Our results show that for a well-calibrated lidar and camera pair with minimal viewpoint misalignment, a simple clustering strategy is sufficient to isolate object points \mathbf{O}_i^T from the set of points in the mask $\mathbf{S}_i^T = \{s_k^T |_{k=1}^{N_k}\}$, where s_k^T is the set of mask points for the k -th object.

VRES-based Clustering. To find the points of the k -th object o_k^T from the point set s_k^T of the i -th point cloud, we employ a DB-Scan [14] clustering strategy using an estimated vertical resolution (VRES) of the lidar. A typical characteristic of lidars is that the separation between points widens with distance. For ring-based lidars, such as KITTI, this widening is more prevalent in the vertical separation between points of different rings as illustrated in Figure 4. Therefore, a good clustering distance ϵ needs to be adaptive to the widening of vertical point distances. We can estimate a VRES ϕ_v with $\phi_v = \frac{\theta_F}{N_R}$, where θ_F is the vertical field-

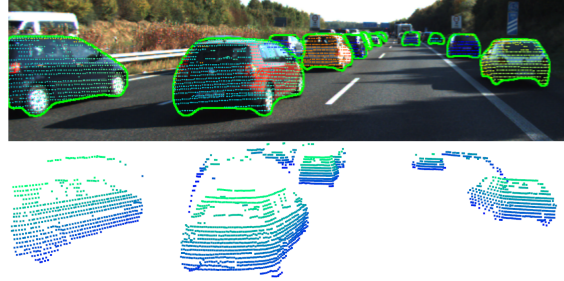


Figure 3. Background points due to viewpoint misalignment in KITTI dataset.

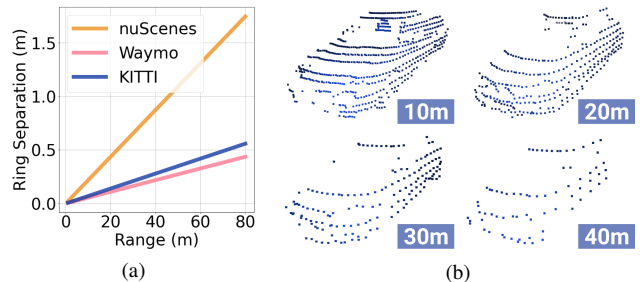


Figure 4. (a) Lidar ring separation with increasing distance. At 40m, the distance between the vertical rings of the nuScenes lidar is nearly 1m, which is more than half the height of most cars; (b) Velodyne HDL-64E (KITTI) ring separation at 10m, 20m, 30m and 40m. A KITTI car at 40m has 0.25m ring separation, which leads to a maximum of 5-6 rings on the car.

of-view (FOV) of the lidar and N_R is the number of rings. For a non-ring based lidar, N_R was approximated based on the observed resolution. The clustering distance ϵ can be set by $\epsilon = \alpha d_v$, where $d_o = \|p_k^T\|_2$ is the centroid distance of the mask points and α is a scaling factor for the vertical point distance $d_v = d_o \tan(\phi_v)$. We select the largest cluster of p_k^T as the set of our object points o_k^T .

3.3. Surface Completion

To recover the geometry of the isolated object points o_k^S and o_k^T , we use the Ball-Pivoting Algorithm (BPA) [3] to interpolate a triangle mesh. The core idea of BPA is simple. A set of spheres are rolled around the point set. If any ball touches three points and doesn't fall through, it forms a triangle. We estimate surface normals for the object point set by orienting them towards the lidar origin. BPA uses these surface normals to ensure that triangles are only generated on the surface of the object; this was effective in recovering an accurate geometry of the object. The added benefit of using an SC method is that we address the issue of partial occlusion, where objects are split into two components, most commonly in driving datasets by poles, signs or trees. With BPA we can connect the two disjointed components

into a single object. We note that this component of our framework can be easily swapped out with other SC methods such as Alpha Shapes [13] or Poisson Surface Reconstruction [23], where the point set does not need to be normalized at the origin with zero rotation (such as [68, 69]).

3.4. Point Sampling

Objects at closer ranges typically have more confident detections due to the high density of points; this can be observed in the Waymo leaderboard [51] when scoring by range. In the last phase of SEE, we choose to upsample every object’s triangle mesh to increase the confidence of 3D detectors. We sample the triangle meshes using Poisson disk sampling [70], where each point is approximately equidistant to neighbouring points.

To increase the confidence of detections at a further range, we upsample the meshes to emulate the point density of objects at a closer range (5-10m). Smaller point distances are typically correlated with a higher density of points. We define an ideal vertical point distance, called optimal ring separation d_{opt} , as our desired density of points. The relationship between d_{opt} and vertical point distance d_v can be represented as $d_{opt} = \frac{d_v}{\beta}$, since d_v increases with distance. By rearranging this equation, we can solve for our upsampling factor β . Whilst more points are generally better, densely sampled points may accentuate mistakes in the object isolation phase. We sample each i -th point cloud object according to this strategy to obtain our semi-canonical representation M_i^S and M_i^T .

3.5. Object Detection in the Semi-Canonical Domain

We train 3D object detectors on the semi-canonical domain $\rho(M_i^S)$ using labels in the source domain Y_i^S . We demonstrate the framework on two SOTA detectors SECOND-IoU [61, 64] and PV-RCNN [46], which required no architectural modifications. Input dimensions had to be modified as SEE only supports (x, y, z) point types (without intensity, velocity, or other properties) at this stage. Given a point cloud in the test domain X_i^T we isolate the objects O_i^T ; convert to the semi-canonical domain M_i^T ; apply the detection network $\rho(M_i^T)$; and finally, project the detections back into the target domain X_i^T .

4. Experiments

In this section, we first validate SEE on public datasets and subsequently demonstrate its efficacy on the novel Baraja Spectrum-Scan™ dataset.

4.1. Datasets

We evaluate our framework on the “Car” class using three public datasets: Waymo [51], KITTI [16] and

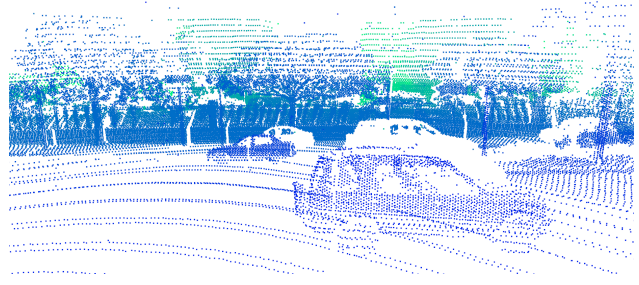


Figure 5. The Baraja Spectrum-Scan™ dataset scan pattern is configured to foveate points at the horizon. The foveation pattern is visible on the SUV where the bottom half has a ring-like appearance whilst the upper half we describe as a uniform, interleaved scan pattern.

nuScenes [6]; and a manually annotated Baraja Spectrum-Scan™ dataset. We demonstrate the concept across multiple scenarios: (1) Differing lidar ring numbers (i.e., nuScenes → KITTI); (2) Multiple concatenated point clouds to a single point cloud (i.e., Waymo → KITTI); (3) Ring-based to a uniform, interleaved scan pattern (i.e., Waymo/nuScenes → Baraja). We evaluate all scenarios on SECOND-IoU [61, 64] and PV-RCNN [46].

KITTI. The KITTI dataset [16] provides 7,481 training samples and 7,518 testing samples. The entire training dataset contains 27,459 cars. The sensor suite includes a 64-beam lidar with 2 colour cameras. Due to the large overlap of camera FOV, we only used one colour camera for the instance segmentation. Objects in KITTI are only annotated if they are visible in the camera FOV. We follow the popular 50/50 training/validation split [10, 61], giving 3,712 training samples and 3,769 validation samples.

nuScenes. The nuScenes dataset [6] provides 28,130 training, 6,019 validation and 6,008 testing samples. The nuScenes sensor suite includes a 32-beam lidar and 6 cameras with 360° coverage. This dataset has a total of 87,249 cars. nuScenes is comprised of 1,000 scenes, each of 20s in length, which gives variety in the observation of objects. For fair comparison across datasets, and due to limited access to hardware resources, we created a subset of the nuScenes training dataset, comprising of 4,025 samples. This subset contains a similar number of cars (27,710 cars) to KITTI. Due to the sparsity of the point cloud (caused by low-resolution 32-beam lidar and wide vertical FOV), we truncated the point cloud range in the training process to [-24, 24]m for X and Y, and [-2, 4]m for Z-axis. Cars further than 24m in nuScenes often have only a single horizontal line of points, which leads to subpar meshes.

Waymo. The Waymo Open Dataset [51] contains 1,000 scenes, each with 200 frames. The dataset provides a top-mounted 64-beam lidar and 4 short-range lidars, with the top-lidar point cloud truncated to a maximum of 75m and short-range at 20m. We concatenate all 5 lidar scans into

Task	Method	SECOND-IoU				PV-RCNN			
		0.7 IoU		0.5 IoU		0.7 IoU		0.5 IoU	
		3D	BEV	3D	BEV	3D	BEV	3D	BEV
nuScenes → KITTI	Oracle	81.73	86.07	89.28	89.29	89.32	92.17	94.97	94.98
	Source-only	16.39	48.74	65.89	72.47	48.03	68.97	77.09	77.71
	ST3D [64]	58.58	76.82	81.19	81.64	70.85*	78.36*	83.64*	83.75*
	SEE	56.00	77.00	88.62	90.70	72.51	85.53	91.68	91.75
	SEE-Ideal	66.82	83.80	92.82	93.49	80.29	89.94	93.74	93.77
	Improvement	+39.61	+28.26	+22.73	+18.23	+24.49	+16.56	+14.59	+14.05
Waymo → KITTI	Oracle	81.73	86.07	89.28	89.29	89.32	92.17	94.97	94.98
	Source-only	11.92	47.67	86.54	90.35	41.54	67.42	84.03	84.46
	ST3D [64]	62.81	78.93	89.08	89.65	73.32	89.94	93.94	93.98
	SEE	65.52	88.09	96.70	96.92	79.39	90.82	96.70	96.82
	SEE-Ideal	70.48	88.93	98.22	98.32	84.49	93.17	98.79	98.85
	Improvement	+53.60	+40.42	+10.16	+6.57	+37.85	+23.41	+12.67	+12.35

Table 1. Results for the different DA scenarios. We report the AP for the car category on KITTI dataset in bird’s-eye-view (AP_{BEV}) and 3D (AP_{3D}) at IoU = 0.7 and 0.5 on the moderate case. “Improvement” denotes the AP increase from Source-only to our proposed, SEE. The best results are indicated in bold. All models are evaluated on ground truth boxes with 50 points or more. Publicly available ST3D models are evaluated with this same criterion. *nuScenes → KITTI results for ST3D with PV-RCNN are from their original paper, evaluated on all ground-truth boxes as the model was not available from the codebase.

a single point cloud for our experimentation. Similar to nuScenes, we create a subset of the Waymo dataset. Selecting one frame from each scene leads to a subset of 1,000 training samples with a similar number of cars (30,405 cars) to the KITTI dataset. We trained the model on the “Vehicle” class with a point cloud range of [-75.2, 75.2]m for X and Y for SECOND-IoU, [-50, 50]m for X and Y for PV-RCNN, and [-2,4]m for Z-axis on both detectors.

Baraja Spectrum-Scan™. Our manually labelled dataset uses Baraja Spectrum-Scan™, a novel, high-resolution lidar that can dynamically increase point cloud resolution around key objects [37]. We foveated the points to focus on the horizon for the specific scenes in our collected dataset as shown in Figure 5. In our particular configuration, the centre of the vertical FOV has a uniform, interleaved distribution of points where the vertical and horizontal angular resolution is approximately equal. The top and bottom of the vertical FOV appear similar to the rings of KITTI, Waymo, and nuScenes. Our camera, Intel RealSense D435i, was mounted directly below the lidar. Using the labelling tool, SUSTechPOINTS [28], we followed the KITTI annotation scheme and labelled cars only if they are visible in the image FOV. In the image extremities, we only label cars if more than 50% of the car is visible in the image. We adopt the same dataset limitations as Waymo in truncating the point cloud to a maximum of 75m, and we include the side mirrors within the annotated bounding box. The dataset was collected in San Francisco during a sunny day and contains 100 frames, with a total of 928 cars.

4.2. SEE Results on Public Datasets

Comparisons. SEE was compared in the UDA scenario where no prior information about the target domain is known. We adopt a similar convention to [64] and compare SEE with (1) Source-only, where no DA strategies are used; (2) ST3D [64], the SOTA UDA method on 3D object detection using self-training. Trained ST3D models were obtained from their open-sourced codebase; (3) SEE-Ideal, where we use the ground truth annotations to isolate the target domain objects; (4) Oracle, the fully supervised detector trained on the target domain. For (3), the ideal case highlights the potential of this framework with further improvements to object isolation, viewpoint alignment and image instance segmentation in the target domain.

Evaluation Metric. We evaluate SEE on the “Car” category in the KITTI validation dataset, similar to other UDA methods [56, 64]. We follow the official KITTI evaluation metric and report the average precision (AP) over 40 recall positions at 0.7 and 0.5 IoU thresholds for both BEV and 3D IoUs. We report the performance increase of models trained with SEE, over the Source-only. We evaluate all methods only on ground truth annotations where there are 50 points or more within the 3D bounding box. This is because when there are less than 50 points, it is often not sufficient to generate a significant triangle mesh [48]. We explore this further in Section 5.

Implementation Details. We use the Hybrid Task Cascade instance segmentation network [7] provided by the mmdetection codebase [9] which was pretrained on the COCO dataset [29]. In our SEE framework, we set $d_{opt} = 0.05$,

Source	Method	SECOND-IoU				PV-RCNN			
		0.7 IOU		0.5 IOU		0.7 IOU		0.5 IOU	
		3D	BEV	3D	BEV	3D	BEV	3D	BEV
nuScenes	Source-only	1.02	5.12	6.53	7.10	10.85	13.74	14.46	14.50
	SEE	34.54	58.45	70.46	73.02	64.34	77.73	83.66	85.72
	Improvement	+33.52	+53.33	+63.92	+65.93	+53.49	+63.99	+69.20	+71.22
Waymo	Source-only	49.96	74.64	84.11	88.03	76.14	84.10	86.67	88.08
	SEE	73.79	84.74	90.36	92.53	79.13	87.79	93.05	93.17
	Improvement	+23.84	+10.10	+6.25	+4.50	+2.98	+3.69	+6.38	+5.09

Table 2. Results for the Baraja Spectrum-ScanTM dataset. ‘‘Improvement’’ denotes the AP increase from Source-only to our proposed, SEE. All results are obtained using the same trained models in Table 1.

$\alpha = 5$, 20 BPA spheres with upper radius 1.155, and we shrink instance segmentation masks by 2%. For cross-dataset training and evaluation, we adopted the settings of the ST3D [64] codebase which was based on OpenPCDet [52]. We add an offset to the z coordinates of nuScenes (+1.8m), KITTI (+1.6m), and Baraja Spectrum-ScanTM (+2.2m) to shift the origin to the ground plane. For training, we use the widely adopted data augmentation strategies: random flipping, random world scaling, random world rotation, and random object scaling (proposed by [64]). See supplementary material for more details.

Results. From Table 1, we show that SEE improves the performance of both detectors by a large margin on all unsupervised DA scenarios. In the nuScenes \rightarrow KITTI, where the number of lidar beams differs, SEE closed the performance gap by 39.61 AP for SECOND-IoU and 24.49 AP for PV-RCNN in AP_{3D}. By upsampling the triangle meshes, SEE gives a strong indication of the presence of objects in the point cloud. This is reflected in the strong performance in the 0.5 IoU threshold, which outperforms ST3D. Due to the nature of our approach, having more points leads to a better-interpolated geometry. This is observed in the Waymo \rightarrow KITTI task, where our approach outperforms ST3D with both SECOND-IoU and PV-RCNN in both IoU thresholds. We note that there is a substantial gap when comparing SEE to SEE-Ideal, which indicates the potential of our chosen SC method, BPA, with improvements to the object isolation phase and future instance segmentation models. We believe that the gap between SEE and SEE-Ideal can be further closed if the camera and lidar viewpoint alignment is minimised, as this reduces background points. These promising results validate the ability of our framework in adapting 3D object detectors from one scan pattern to another.

4.3. SEE for Baraja Spectrum-ScanTM

In Table 2, we prove the industry applications of our framework by evaluating on the Baraja Spectrum-ScanTM dataset. We demonstrate that the same trained models in Table 1 can attain high performance in an unseen dataset

with a distinct scan pattern (see Figure 5). When comparing with nuScenes, due to its ring-like nature and sparsity of beams, the scan pattern of the lidar is vastly different. Even at a close range, a car in nuScenes bears little resemblance to any car perceived by Baraja Spectrum-ScanTM. In Table 2, this is observed in the dramatically low performance of models trained on nuScenes as the source domain, obtaining 1.02 and 10.85 in AP_{3D} for SECOND-IoU and PV-RCNN respectively. When the same models are trained with SEE, the performance is drastically improved with an increase of 1.02 \rightarrow 34.54 and 10.85 \rightarrow 64.34 in AP_{3D}. For Waymo, lidar beams are clustered in the middle of vertical angles, leading to high resolution at the horizon and sparse rings in the top and bottom of the FOV, similar to Baraja Spectrum-ScanTM. This scan pattern similarity leads to a higher performing ‘‘Source-only’’. We note that for the Waymo ‘‘Source-only’’ PV-RCNN, whilst obtaining a high performance on Baraja Spectrum-ScanTM, it does not perform well on KITTI as shown in Table 1. We show that a SEE-trained detector can obtain high performance on both KITTI and Baraja Spectrum-ScanTM and for this dataset, further push the performance to 73.79 and 79.13 in AP_{3D} at 0.7 IoU for SECOND-IoU and PV-RCNN respectively. In the supplementary material, we qualitatively show that our SEE framework leads to less false positive detections and better rotation estimation.

5. Ablation Studies

In this section, we conduct ablation studies using the SECOND-IoU model.

Minimum number of points. To interpolate the underlying geometry, we need to have a sufficient amount of points to interpolate from. We investigate the performance of SEE on objects containing less than 50 points and adjust the evaluation accordingly. For example, if the minimum number of points for the SC phase is 40, we also evaluate only on all ground-truth boxes that have 40 points or more. It can be seen in Figure 6, evaluated on SEE-Ideal in the Waymo \rightarrow KITTI scenario, that having more points leads to higher

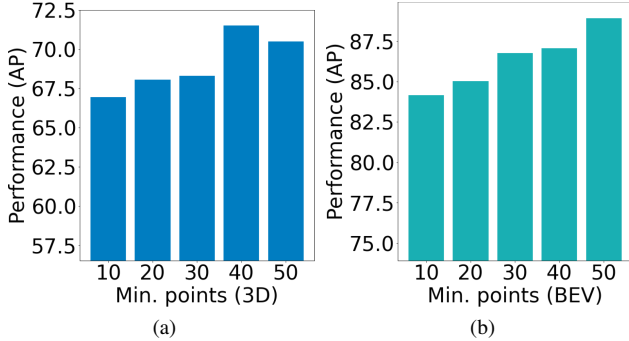


Figure 6. Minimum number of points using SEE-Ideal, evaluated on the Waymo → KITTI scenario with SECOND-IoU. Reported AP is on 0.7 IoU threshold for (a) 3D (b) BEV. Only objects with points greater than “Min. Points” are processed by SEE.

quality meshes, and hence, better detection performance.

Point Sampling Strategy. We compare our VRES-based sampling with two other strategies: (1) Surface-area (SA) based sampling, where we sample a certain number of points per m^2 of the triangle mesh surface area; (2) Virtual lidar (VL), where we adopt the strategy of [66] mimicking the scan pattern of the target domain by comparing the spherical coordinates of the point clouds. In Table 3 we can see that a increasing the density of point sampling in $d_{opt} = 0.03$ and $\frac{pts}{m^2} = 700$ causes a decrease in performance, as it potentially over-accentuates mistakes of the SC method. On the flip side, fewer points lead to a weaker presence of the object, which also decreases the performance. The VL strategy is comparable with VRES-based strategy, making it a promising alternative.

Surface completion. We compare with another SC method, Alpha Shapes [13] in Table 4. For Alpha Shapes, it tends to join the interior object points, leading to irregularly shaped cars. We used linear regression to identify the optimal alpha to generate for objects at various ranges. We define the optimal alpha value as the maximum number of fitted triangle vertices. It can be seen that the performance degrades when using Alpha Shapes over BPA.

6. Discussion and Future Work

Whilst high-performing, our framework does not run in real-time. Regardless, it is computationally easier to adopt novel, unique types of lidars with SEE as model training is not required; instance segmentation inference and surface completion (including deep learning-based ones) are not as intensive. As previously shown in Figure 6, our method performs better with more points on the object. We, however, consider this a minor limitation as we argue that the future direction of lidar manufacturing is headed towards higher resolution point clouds. The results in Table 4 indicates the importance of the surface completion phase and

Strategy	Config	3D	BEV
VRES (d_{opt})	0.07	64.13 / 58.70	85.70 / 82.36
	0.05	70.96 / 65.52	89.70 / 88.09
	0.03	68.62 / 57.16	89.50 / 87.94
SA ($\frac{pts}{m^2}$)	300	70.86 / 58.70	89.67 / 80.68
	500	75.52 / 61.41	91.17 / 80.34
	700	73.86 / 61.80	89.63 / 81.09
VL	-	70.02 / 64.23	86.71 / 85.57

Table 3. Point sampling strategies: VRES, Surface-Area (SA), and Virtual Lidar (VL), for sampling from the mesh in phase 3 of SEE. Reported AP shows SEE-Ideal / SEE for the 0.7 IoU threshold using SECOND-IoU on the Waymo → KITTI task. Methods are evaluated on ground truth boxes with 50 or more points.

Surface Completion		3D	BEV
BPA	SEE-Ideal	66.81	82.67
	SEE	55.78	76.80
Alpha Shapes	SEE-Ideal	56.31	68.57
	SEE	49.07	65.17

Table 4. Comparison of BPA with Alpha Shapes. Reported AP is on the nuScenes → KITTI task with SECOND-IoU at 0.7 IoU.

leads us to believe that better surface completion methods can further improve the domain adaptation capabilities of SEE. Furthermore, we believe that there is potential in our framework to adopt deep learning approaches in our surface completion phase. The difficulty in naively adopting deep learning shape completion methods [48, 68, 69], however, is that they often require the ground truth boxes to translate object points to the origin, reset to 0 rotation, and scale down the points using bounding box dimensions. Errors in initial point estimation or translation/rotation can cause the shape completion network to generate spurious cars in odd rotations and positions; this is detrimental to the 3D detection network. Please refer to our supplementary material for more details on shape completion in SEE. Future work on SEE will explore different in-place surface completion methods and solutions for normalizing the object to enable direct adoption of deep learning shape completion methods.

7. Conclusion

We present SEE, a lidar-agnostic 3D object detection framework for adapting the performance of a detector trained on one scan pattern, to any other scan pattern. SEE allows easy adoption of novel, unique types of lidars without requiring fine-tuning of the model. We demonstrate that the scan pattern discrepancy is a large component of the domain gap. Extensive experiments on public datasets and a novel, unique lidar dataset validate the efficacy and industry applicability of our framework.

References

- [1] Idan Achituve, Haggai Maron, and Gal Chechik. Self-supervised learning for domain adaptation on point clouds. In *Proceedings of the IEEE/CVF Winter Conference on Applications of Computer Vision*, pages 123–133, 2021. 3
- [2] Inigo Alonso, Luis Riazuelo Montesano, Ana C Murillo, et al. Domain adaptation in lidar semantic segmentation. *arXiv preprint arXiv:2010.12239*, 2020. 3
- [3] Fausto Bernardini, Joshua Mittleman, Holly Rushmeier, Claudio Silva, and Gabriel Taubin. The ball-pivoting algorithm for surface reconstruction. *IEEE transactions on visualization and computer graphics*, 5(4):349–359, 1999. 2, 4
- [4] Julie Stephany Berrio, Mao Shan, Stewart Worrall, and Eduardo Nebot. Camera-lidar integration: Probabilistic sensor fusion for semantic mapping. *IEEE Transactions on Intelligent Transportation Systems*, pages 1–16, 2021. 4
- [5] Konstantinos Bousmalis, Nathan Silberman, David Dohan, Dumitru Erhan, and Dilip Krishnan. Unsupervised pixel-level domain adaptation with generative adversarial networks. In *Proceedings of the IEEE conference on computer vision and pattern recognition*, pages 3722–3731, 2017. 3
- [6] Holger Caesar, Varun Bankiti, Alex H Lang, Sourabh Vora, Venice Erin Liong, Qiang Xu, Anush Krishnan, Yu Pan, Giancarlo Baldan, and Oscar Beijbom. nuscenes: A multi-modal dataset for autonomous driving. In *Proceedings of the IEEE/CVF conference on computer vision and pattern recognition*, pages 11621–11631, 2020. 1, 5
- [7] Kai Chen, Jiangmiao Pang, Jiaqi Wang, Yu Xiong, Xiaoxiao Li, Shuyang Sun, Wansen Feng, Ziwei Liu, Jianping Shi, Wanli Ouyang, Chen Change Loy, and Dahua Lin. Hybrid task cascade for instance segmentation. In *IEEE Conference on Computer Vision and Pattern Recognition*, 2019. 6
- [8] Ke Chen and Ahmad Salman. Extracting speaker-specific information with a regularized siamese deep network. In *NIPS*, volume 2011, pages 298–306, 2011. 3
- [9] Kai Chen, Jiaqi Wang, Jiangmiao Pang, Yuhang Cao, Yu Xiong, Xiaoxiao Li, Shuyang Sun, Wansen Feng, Ziwei Liu, Jiarui Xu, Zheng Zhang, Dazhi Cheng, Chenchen Zhu, Tianheng Cheng, Qijie Zhao, Buyu Li, Xin Lu, Rui Zhu, Yue Wu, Jifeng Dai, Jingdong Wang, Jianping Shi, Wanli Ouyang, Chen Change Loy, and Dahua Lin. MMDetection: Open mmlab detection toolbox and benchmark. *arXiv preprint arXiv:1906.07155*, 2019. 6
- [10] Xiaozhi Chen, Huimin Ma, Ji Wan, Bo Li, and Tian Xia. Multi-view 3d object detection network for autonomous driving. In *Proceedings of the IEEE conference on Computer Vision and Pattern Recognition*, pages 1907–1915, 2017. 3, 5
- [11] Jiajun Deng, Shaoshuai Shi, Peiwei Li, Wengang Zhou, Yanyong Zhang, and Houqiang Li. Voxel r-cnn: Towards high performance voxel-based 3d object detection. *arXiv preprint arXiv:2012.15712*, 2020. 3
- [12] Xinxin Du, Marcelo H Ang, Sertac Karaman, and Daniela Rus. A general pipeline for 3d detection of vehicles. In *2018 IEEE International Conference on Robotics and Automation (ICRA)*, pages 3194–3200. IEEE, 2018. 3
- [13] Herbert Edelsbrunner, David Kirkpatrick, and Raimund Seidel. On the shape of a set of points in the plane. *IEEE Transactions on information theory*, 29(4):551–559, 1983. 5, 8
- [14] Martin Ester, Hans-Peter Kriegel, Jörg Sander, Xiaowei Xu, et al. A density-based algorithm for discovering clusters in large spatial databases with noise. In *kdd*, volume 96, pages 226–231, 1996. 4
- [15] Yaroslav Ganin, Evgeniya Ustinova, Hana Ajakan, Pascal Germain, Hugo Larochelle, François Laviolette, Mario Marchand, and Victor Lempitsky. Domain-adversarial training of neural networks. *The journal of machine learning research*, 17(1):2096–2030, 2016. 3
- [16] Andreas Geiger, Philip Lenz, and Raquel Urtasun. Are we ready for autonomous driving? the kitti vision benchmark suite. In *2012 IEEE conference on computer vision and pattern recognition*, pages 3354–3361. IEEE, 2012. 1, 2, 5
- [17] Francisco Gomez-Donoso, Edmanuel Cruz, Miguel Cazorla, Stewart Worrall, and Eduardo Nebot. Using a 3d cnn for rejecting false positives on pedestrian detection. In *2020 International Joint Conference on Neural Networks (IJCNN)*, pages 1–6. IEEE, 2020. 4
- [18] Arthur Gretton, Karsten Borgwardt, Malte Rasch, Bernhard Schölkopf, and Alex Smola. A kernel method for the two-sample-problem. *Advances in neural information processing systems*, 19:513–520, 2006. 3
- [19] Chenhang He, Hui Zeng, Jianqiang Huang, Xian-Sheng Hua, and Lei Zhang. Structure aware single-stage 3d object detection from point cloud. In *Proceedings of the IEEE/CVF Conference on Computer Vision and Pattern Recognition*, pages 11873–11882, 2020. 1
- [20] Weixiang Hong, Zhenzhen Wang, Ming Yang, and Junsong Yuan. Conditional generative adversarial network for structured domain adaptation. In *Proceedings of the IEEE Conference on Computer Vision and Pattern Recognition*, pages 1335–1344, 2018. 3
- [21] Maximilian Jaritz, Tuan-Hung Vu, Raoul de Charette, Emilie Wirbel, and Patrick Pérez. xmuda: Cross-modal unsupervised domain adaptation for 3d semantic segmentation. In *Proceedings of the IEEE/CVF Conference on Computer Vision and Pattern Recognition*, pages 12605–12614, 2020. 3
- [22] Guoliang Kang, Lu Jiang, Yi Yang, and Alexander G Hauptmann. Contrastive adaptation network for unsupervised domain adaptation. In *Proceedings of the IEEE/CVF Conference on Computer Vision and Pattern Recognition*, pages 4893–4902, 2019. 3
- [23] Michael Kazhdan, Matthew Bolitho, and Hugues Hoppe. Poisson surface reconstruction. In *Proceedings of the fourth Eurographics symposium on Geometry processing*, volume 7, 2006. 5
- [24] Jason Ku, Melissa Mozifian, Jungwook Lee, Ali Harakeh, and Steven L Waslander. Joint 3d proposal generation and object detection from view aggregation. In *2018 IEEE/RSJ International Conference on Intelligent Robots and Systems (IROS)*, pages 1–8. IEEE, 2018. 3
- [25] Alex H Lang, Sourabh Vora, Holger Caesar, Lubing Zhou, Jiong Yang, and Oscar Beijbom. Pointpillars: Fast encoders

- for object detection from point clouds. In *Proceedings of the IEEE/CVF Conference on Computer Vision and Pattern Recognition*, pages 12697–12705, 2019. 3
- [26] Ferdinand Langer, Andres Milioto, Alexandre Haag, Jens Behley, and Cyrill Stachniss. Domain transfer for semantic segmentation of lidar data using deep neural networks. In *2020 IEEE/RSJ International Conference on Intelligent Robots and Systems (IROS)*, pages 8263–8270. IEEE, 2020. 3
- [27] Bo Li. 3d fully convolutional network for vehicle detection in point cloud. In *2017 IEEE/RSJ International Conference on Intelligent Robots and Systems (IROS)*, pages 1513–1518. IEEE, 2017. 3
- [28] E Li, Shuaijun Wang, Chengyang Li, Dachuan Li, Xiangbin Wu, and Qi Hao. Sustech points: A portable 3d point cloud interactive annotation platform system. In *2020 IEEE Intelligent Vehicles Symposium (IV)*, pages 1108–1115, 2020. 6
- [29] Tsung-Yi Lin, Michael Maire, Serge Belongie, James Hays, Pietro Perona, Deva Ramanan, Piotr Dollár, and C Lawrence Zitnick. Microsoft coco: Common objects in context. In *European conference on computer vision*, pages 740–755. Springer, 2014. 6
- [30] Ming-Yu Liu and Oncel Tuzel. Coupled generative adversarial networks. *Advances in neural information processing systems*, 29:469–477, 2016. 3
- [31] Mingsheng Long, Yue Cao, Jianmin Wang, and Michael Jordan. Learning transferable features with deep adaptation networks. In *International conference on machine learning*, pages 97–105. PMLR, 2015. 3
- [32] Jiageng Mao, Minzhe Niu, Haoyue Bai, Xiaodan Liang, Hang Xu, and Chunjing Xu. Pyramid r-cnn: Towards better performance and adaptability for 3d object detection. In *Proceedings of the IEEE/CVF International Conference on Computer Vision*, pages 2723–2732, 2021. 3
- [33] Jiageng Mao, Yujing Xue, Minzhe Niu, Haoyue Bai, Jiashi Feng, Xiaodan Liang, Hang Xu, and Chunjing Xu. Voxel transformer for 3d object detection. In *Proceedings of the IEEE/CVF International Conference on Computer Vision*, pages 3164–3173, 2021. 3
- [34] Pietro Morerio and Vittorio Murino. Correlation alignment by riemannian metric for domain adaptation. *arXiv preprint arXiv:1705.08180*, 2017. 3
- [35] Xuran Pan, Zhuofan Xia, Shiji Song, Li Erran Li, and Gao Huang. 3d object detection with pointformer. In *Proceedings of the IEEE/CVF Conference on Computer Vision and Pattern Recognition*, pages 7463–7472, 2021. 3
- [36] Su Pang, Daniel Morris, and Hayder Radha. Cloccs: Camera-lidar object candidates fusion for 3d object detection. In *2020 IEEE/RSJ International Conference on Intelligent Robots and Systems (IROS)*, pages 10386–10393. IEEE, 2020. 3
- [37] Cibby Pulikkaseril and Nick Langdale-Smith. Next generation lidar for a fully autonomous future. <https://www.baraja.com/en/technology/white-paper>, 2020. 6
- [38] Charles R Qi, Wei Liu, Chenxia Wu, Hao Su, and Leonidas J Guibas. Frustum pointnets for 3d object detection from rgb-d data. In *Proceedings of the IEEE conference on computer vision and pattern recognition*, pages 918–927, 2018. 3
- [39] Charles R Qi, Hao Su, Kaichun Mo, and Leonidas J Guibas. Pointnet: Deep learning on point sets for 3d classification and segmentation. In *Proceedings of the IEEE conference on computer vision and pattern recognition*, pages 652–660, 2017. 3
- [40] Charles R Qi, Li Yi, Hao Su, and Leonidas J Guibas. Pointnet++: Deep hierarchical feature learning on point sets in a metric space. *arXiv preprint arXiv:1706.02413*, 2017. 3
- [41] Can Qin, Haoxuan You, Lichen Wang, C-C Jay Kuo, and Yun Fu. Pointdan: A multi-scale 3d domain adaption network for point cloud representation. *arXiv preprint arXiv:1911.02744*, 2019. 3
- [42] Artem Rozantsev, Mathieu Salzmann, and Pascal Fua. Beyond sharing weights for deep domain adaptation. *IEEE transactions on pattern analysis and machine intelligence*, 41(4):801–814, 2018. 3
- [43] Cristiano Saltori, Stéphane Lathuilière, Nicu Sebe, Elisa Ricci, and Fabio Galasso. Sf-uda 3d: Source-free unsupervised domain adaptation for lidar-based 3d object detection. In *2020 International Conference on 3D Vision (3DV)*, pages 771–780. IEEE, 2020. 3
- [44] Swami Sankaranarayanan, Yogesh Balaji, Carlos D Castillo, and Rama Chellappa. Generate to adapt: Aligning domains using generative adversarial networks. In *Proceedings of the IEEE Conference on Computer Vision and Pattern Recognition*, pages 8503–8512, 2018. 3
- [45] Jian Shen, Yanru Qu, Weinan Zhang, and Yong Yu. Wasserstein distance guided representation learning for domain adaptation. In *Thirty-Second AAAI Conference on Artificial Intelligence*, 2018. 3
- [46] Shaoshuai Shi, Chaoxu Guo, Li Jiang, Zhe Wang, Jianping Shi, Xiaogang Wang, and Hongsheng Li. Pv-rcnn: Point-voxel feature set abstraction for 3d object detection. In *Proceedings of the IEEE/CVF Conference on Computer Vision and Pattern Recognition*, pages 10529–10538, 2020. 1, 2, 3, 5
- [47] Shaoshuai Shi, Xiaogang Wang, and Hongsheng Li. Point-rcnn: 3d object proposal generation and detection from point cloud. In *Proceedings of the IEEE/CVF conference on computer vision and pattern recognition*, pages 770–779, 2019. 3
- [48] David Stutz and Andreas Geiger. Learning 3d shape completion from laser scan data with weak supervision. In *Proceedings of the IEEE Conference on Computer Vision and Pattern Recognition*, pages 1955–1964, 2018. 6, 8
- [49] Baochen Sun, Jiashi Feng, and Kate Saenko. Return of frustratingly easy domain adaptation. In *Proceedings of the AAAI Conference on Artificial Intelligence*, volume 30, 2016. 3
- [50] Baochen Sun and Kate Saenko. Deep coral: Correlation alignment for deep domain adaptation. In *European conference on computer vision*, pages 443–450. Springer, 2016. 3
- [51] Pei Sun, Henrik Kretschmar, Xerxes Dotiwalla, Aurelien Chouard, Vijaysai Patnaik, Paul Tsui, James Guo, Yin Zhou, Yuning Chai, Benjamin Caine, et al. Scalability in perception for autonomous driving: Waymo open dataset. In *Proceedings of the IEEE/CVF Conference on Computer Vision and Pattern Recognition*, pages 2446–2454, 2020. 1, 2, 5

- [52] OpenPCDet Development Team. Openpcdet: An open-source toolbox for 3d object detection from point clouds. <https://github.com/open-mmlab/OpenPCDet>, 2020. 7
- [53] Darren Tsai, Stewart Worrall, Mao Shan, Anton Lohr, and Eduardo Nebot. Optimising the selection of samples for robust lidar camera calibration. In *2021 IEEE International Intelligent Transportation Systems Conference (ITSC)*, pages 2631–2638, 2021. 4
- [54] Eric Tzeng, Judy Hoffman, Kate Saenko, and Trevor Darrell. Adversarial discriminative domain adaptation. In *Proceedings of the IEEE conference on computer vision and pattern recognition*, pages 7167–7176, 2017. 3
- [55] Sourabh Vora, Alex H Lang, Bassam Helou, and Oscar Beijbom. Pointpainting: Sequential fusion for 3d object detection. In *Proceedings of the IEEE/CVF conference on computer vision and pattern recognition*, pages 4604–4612, 2020. 3
- [56] Yan Wang, Xiangyu Chen, Yurong You, Li Erran Li, Bharath Hariharan, Mark Campbell, Kilian Q Weinberger, and Wei-Lun Chao. Train in germany, test in the usa: Making 3d object detectors generalize. In *Proceedings of the IEEE/CVF Conference on Computer Vision and Pattern Recognition*, pages 11713–11723, 2020. 3, 6
- [57] Yifei Wang, Wen Li, Dengxin Dai, and Luc Van Gool. Deep domain adaptation by geodesic distance minimization. In *Proceedings of the IEEE International Conference on Computer Vision Workshops*, pages 2651–2657, 2017. 3
- [58] Zhixin Wang and Kui Jia. Frustum convnet: Sliding frustums to aggregate local point-wise features for amodal 3d object detection. In *2019 IEEE/RSJ International Conference on Intelligent Robots and Systems (IROS)*, pages 1742–1749. IEEE, 2019. 3
- [59] Bichen Wu, Xuanyu Zhou, Sicheng Zhao, Xiangyu Yue, and Kurt Keutzer. Squeezesegv2: Improved model structure and unsupervised domain adaptation for road-object segmentation from a lidar point cloud. In *2019 International Conference on Robotics and Automation (ICRA)*, pages 4376–4382. IEEE, 2019. 3
- [60] Qiangeng Xu, Yin Zhou, Weiyue Wang, Charles R Qi, and Dragomir Anguelov. Spg: Unsupervised domain adaptation for 3d object detection via semantic point generation. In *Proceedings of the IEEE/CVF International Conference on Computer Vision*, pages 15446–15456, 2021. 3
- [61] Yan Yan, Yuxing Mao, and Bo Li. Second: Sparsely embedded convolutional detection. *Sensors*, 18(10):3337, 2018. 2, 3, 5
- [62] Bin Yang, Wenjie Luo, and Raquel Urtasun. Pixor: Real-time 3d object detection from point clouds. In *Proceedings of the IEEE conference on Computer Vision and Pattern Recognition*, pages 7652–7660, 2018. 3
- [63] Jihan Yang, Shaoshuai Shi, Zhe Wang, Hongsheng Li, and Xiaojuan Qi. St3d++: Denoised self-training for unsupervised domain adaptation on 3d object detection. *arXiv preprint arXiv:2108.06682*, 2021. 3
- [64] Jihan Yang, Shaoshuai Shi, Zhe Wang, Hongsheng Li, and Xiaojuan Qi. St3d: Self-training for unsupervised domain adaptation on 3d object detection. In *Proceedings of the IEEE/CVF Conference on Computer Vision and Pattern Recognition*, pages 10368–10378, 2021. 1, 2, 3, 5, 6, 7
- [65] Maosheng Ye, Shuangjie Xu, and Tongyi Cao. Hynet: Hybrid voxel network for lidar based 3d object detection. In *Proceedings of the IEEE/CVF conference on computer vision and pattern recognition*, pages 1631–1640, 2020. 3
- [66] Li Yi, Boqing Gong, and Thomas Funkhouser. Complete & label: A domain adaptation approach to semantic segmentation of lidar point clouds. In *Proceedings of the IEEE/CVF Conference on Computer Vision and Pattern Recognition*, pages 15363–15373, 2021. 1, 3, 8
- [67] Yurong You, Carlos Andres Diaz-Ruiz, Yan Wang, Wei-Lun Chao, Bharath Hariharan, Mark Campbell, and Kilian Q Weinberger. Exploiting playbacks in unsupervised domain adaptation for 3d object detection. *arXiv preprint arXiv:2103.14198*, 2021. 3
- [68] Xumin Yu, Yongming Rao, Ziyi Wang, Zuyan Liu, Jiwen Lu, and Jie Zhou. PointR: Diverse point cloud completion with geometry-aware transformers. In *Proceedings of the IEEE/CVF International Conference on Computer Vision*, pages 12498–12507, 2021. 5, 8
- [69] Wentao Yuan, Tejas Khot, David Held, Christoph Mertz, and Martial Hebert. Pcn: Point completion network. In *2018 International Conference on 3D Vision (3DV)*, pages 728–737. IEEE, 2018. 5, 8
- [70] Cem Yuksel. Sample elimination for generating poisson disk sample sets. In *Computer Graphics Forum*, volume 34, pages 25–32. Wiley Online Library, 2015. 2, 5
- [71] Weichen Zhang, Wen Li, and Dong Xu. Srdan: Scale-aware and range-aware domain adaptation network for cross-dataset 3d object detection. In *Proceedings of the IEEE/CVF Conference on Computer Vision and Pattern Recognition*, pages 6769–6779, 2021. 1, 3
- [72] Yun Zhang, Nianbin Wang, Shaobin Cai, and Lei Song. Unsupervised domain adaptation by mapped correlation alignment. *IEEE Access*, 6:44698–44706, 2018. 3
- [73] Sicheng Zhao, Yezhen Wang, Bo Li, Bichen Wu, Yang Gao, Pengfei Xu, Trevor Darrell, and Kurt Keutzer. epointda: An end-to-end simulation-to-real domain adaptation framework for lidar point cloud segmentation. *arXiv preprint arXiv:2009.03456*, 2, 2020. 3
- [74] Yin Zhou and Oncel Tuzel. Voxnet: End-to-end learning for point cloud based 3d object detection. In *Proceedings of the IEEE conference on computer vision and pattern recognition*, pages 4490–4499, 2018. 3